Numerical simulations of two-dimensional foam by the immersed boundary method

Yongsam Kim [a],*, Ming-Chih Lai [b], Charles S. Peskin [c]

[a] Department of Mathematics, Chung-Ang University, Dongjakgu Heukseokdong, Seoul 156-756, Republic of Korea
[b] Center of Mathematical Modeling and Scientific Computing and Department of Applied Mathematics, National Chiao Tung University, 1001, Ta Hsueh Road, Hsinchu 300, Taiwan
[c] Courant Institute of Mathematical Sciences, New York University, 251 Mercer Street, New York, NY 10012, USA

ARTICLE INFO

ABSTRACT

In this paper, we present an immersed boundary (IB) method to simulate a dry foam, i.e., a foam in which most of the volume is attributed to its gas phase. Dry foam dynamics involves the interaction between a gas and a collection of thin liquid-film internal boundaries that partition the gas into discrete cells or bubbles. The liquid-film boundaries are flexible, contract under the influence of surface tension, and are permeable to the gas, which moves across them by diffusion at a rate proportional to the local pressure difference across the boundary. Such problems are conventionally studied by assuming that the pressure is uniform within each bubble. Here, we introduce instead an IB method that takes into account the non-equilibrium fluid mechanics of the gas. To model gas diffusion across the internal liquid-film boundaries, we allow normal slip between the boundary and the gas at a velocity proportional to the (normal) force generated by the boundary surface tension. We implement this method in the two-dimensional case, and test it by verifying the von Neumann relation, which governs the coarsening of a two-dimensional dry foam. The method is further validated by a convergence study, which confirms its first-order accuracy.

© 2010 Elsevier Inc. All rights reserved.

1. Introduction

Liquid foams appear in daily life as the soap froth in a washing bowl or the head on a pint of bear. A foam is a gas–liquid mixture in which the volume of liquid is considerably smaller than that of the gas. Usually, in a "wet" foam (for which the volume of fraction of liquid is about 10–20%), the bubbles are approximately spherical; while in a "dry" foam (for which the volume of fraction of liquid is less than 10%), the bubbles are more nearly polyhedral in shape. One interesting phenomenon, which is called diffusive coarsening, is the evolution in bubble size and topological structure that occurs as a result of gas exchange between bubbles [1]. This gas exchange occurs by diffusion through the thin liquid films that separate one bubble from another. The diffusive flux of gas through such a film is proportional to the pressure difference between the two bubbles that are separated by that film.

In 1952, von Neumann [2] showed that the rate of change of the area of a given bubble (a curved polygon) in a two-dimensional dry foam is independent of bubble size and solely dependent on the number of walls (or edges) of the bubble.

---

* Corresponding author. Tel.: +82 2 820 5219; fax: +82 2 823 5214.
E-mail addresses: kimy@cau.ac.kr (Y. Kim), mclai@math.nctu.edu.tw (M.-C. Lai), peskin@cims.nyu.edu (C.S. Peskin).

We give a derivation of von Neumann's result here, since it plays such a large role in the validation of our methodology, and it is therefore important to understand under what conditions the von Neumann relation can be expected to apply. The derivation is based on the fact that the net rate of outward diffusion of gas per unit length through a wall of the (two-dimensional) bubble is proportional to the pressure difference across that wall, which in turn is equal to the product of the surface tension γ and the curvature κ, where κ is considered positive if the wall is concave towards the bubble in question, so that the pressure difference is tending to drive gas out of the bubble. This gives the equation

$$\frac{dA}{dt} = -M\gamma \int_{\Gamma} \kappa dl, \tag{1}$$

where M is a permeability coefficient, the curve Γ is the closed boundary of the bubble, and dl is the arc length along Γ. Since κ is the rate of change of tangent angle along each wall, and since the boundary of the bubble is a closed curve, we also have

$$\int_{\Gamma} \kappa dl + \sum_{i=1}^{n} \alpha_i = 2\pi, \tag{2}$$

where α_i is the exterior angle (i.e., the angle through which the tangent vector turns) at the ith vertex, and n is the number of vertices (which of course is equal to the number of edges) of the bubble.

Considering now only the generic case in which three edges meet at each bubble vertex, and noting that mechanical equilibrium of the massless vertex under surface tension requires that these three edges make equal angles, we conclude that each of the exterior angles must be equal to $2\pi/6$. This makes the sum of the exterior angles be $2\pi n/6$. Combining all of these results, we conclude along with von Neumann that

$$dA/dt = -2\pi M\gamma \left(1 - \frac{n}{6}\right). \tag{3}$$

Note in particular that the area is constant for 6-sided bubbles, that bubbles with fewer than 6 sides tend to disappear (and in fact reach zero area in finite time), and that bubbles with more than 6 sides tend to grow; hence the "coarsening" of the foam, in which bubbles with large numbers of sides grow at the expense of bubbles with small numbers of sides.

The above derivation is remarkably general. In particular it does *not* require that κ be constant along each boundary of the bubble. Thus it applies to foams that are not in mechanical equilibrium, as well as to foams that are. This may not be well known, since the von Neumann condition is generally applied to the equilibrium case, in which each edge is a circular arc.

A similar derivation of the von Neumann relation based on polar coordinates can be found in [3]. Only very recently, the von Neumann relation has been generalized to three-dimensional foams in [4,5].

There are only a few papers in the literature that describe the simulation of foam dynamics in two or in three dimensions. In [1,6], the authors simulated the evolution of a two-dimensional dry foam within the framework of the following assumptions: (i) the Laplace-Young condition that the pressure difference across a bubble wall equals the surface tension times the curvature; (ii) Plateau's rule that the number of walls that meet at each vertex is three and that the angles at these triple junctions are all equal to $2\pi/3$; and (iii) the von Neumann relation for the rate of change of area as derived above. In those simulations, the unknown variables were only the pressure in each bubble (which was uniform within any one bubble, by hypothesis) and the coordinates of the vertices.

There are other foam simulations that take the fluid dynamics into account. In [7], a numerical study based on boundary integral formulation is presented to simulate two-dimensional, doubly periodic, diluted and concentrated emulsions or foams structures in a simple shear Stokes flow. The numerical results show qualitative agreement with theory regarding the basic geometrical features of the evolving microstructure. Recent work of Bazhlekov et al. [8] used a nonsingular boundary integral method to simulate the three-dimensional wet foam drop formation and its dynamics in simple shear flow. The authors also add the disjoining pressure into the interfacial forces so that the repulsive van der Waals forces within small interface-to-interface distances are taken into account. More numerical works on the two- and three-dimensional dry or wet foams can also be found in the Ref. [9]. Unlike the previous literature, the main purpose of the present paper is to describe an immersed boundary (IB) method for the two-dimensional dry foam problem, and to check the von Neumann law in a full Navier–Stokes flow setting.

As discussed before, a foam is divided into bubbles, which we refer to as "cells" from now on. In a dry foam, the walls between the cells are thin, and we idealize these thin walls as massless internal boundaries. These boundaries interact with the gas phase of the foam, which we model as a viscous incompressible fluid of uniform density. This model is reasonable because (i) the pressure differences within the foam are very slight in comparison to the total pressure, and (ii) the flow velocities are very low in comparison to the speed of sound. The interaction between the boundaries and the fluid has three aspects, all of which are taken into account in our methodology. First, the boundaries move at the local fluid velocity. This is the no-slip condition of a viscous fluid (but see below). Second, the boundaries are under surface tension. When curved, they apply a normal force to the fluid in which they are immersed, and thereby generate a jump in pressure across each such boundary. Finally, the boundaries are permeable to the gas, which leaks through them by diffusion with a flux proportional to the pressure difference. This requires a modification of the no-slip condition in the normal direction, but the tangential no-slip condition is maintained despite the boundary permeability.

The IB method that we use to handle porosity is described in [10], in which a 2D parachute with a porous canopy was studied, and it was shown that canopy porosity can help to stabilize the parachute motion. In that work, the parachute

canopy was allowed to slip relative to the fluid, in the normal direction only, at a velocity proportional to the pressure difference across the boundary. Fortunately, it was unnecessary to evaluate the pressure difference explicitly, since the pressure difference is determined by the normal component of the boundary force, and the boundary force is always calculated anyway, from the spatial configuration of the boundary, when the IB method is applied. Thus, in the parachute calculation, the relative slip velocity was obtained from the projection of the boundary force onto the normal direction to the boundary. We use the same method here, with one important simplification. Since the surface tension is uniform, the force that it generates is already normal to the boundary. This means that we can use the boundary force directly, without having to project it and without having to evaluate separately the normal direction.

The rest of the paper is organized as follows. In Section 2, we describe the equations of motion of the foam in immersed boundary form. These are the typical IB equations of motion, generalized to handle a permeable boundary under surface tension. The numerical implementation including external boundary conditions is described in Section 3. In Section 4, we present simulation results: First, we validate the method by checking that the von Neumann relation is satisfied and also by doing a convergence study. Then we consider more complicated cases including one in which significantly non-equilibrium flows of gas occur within each cell of the foam, thus requiring the full fluid dynamics treatment of the present paper. Conclusions and future work are discussed in Section 5.

2. Immersed boundary formulation

In this section, we state the equations of motion of a two-dimensional dry foam, in which the boundaries between cells are idealized as massless curves under a constant surface tension γ. These boundaries are assumed permeable to the gas phase of the foam, with permeability coefficient M. The gas phase is modeled as a viscous incompressible fluid, for reasons that have been stated in the previous section. The constant density and viscosity of the gas are denoted ρ and μ, respectively.

In the following formulation, the parameter s labels a material point of an internal foam boundary. Note that s does not measure arc length, since the distance along the boundary between two particular material points may change over time. We assume that distinct intervals of the parameter s are used for the different internal foam boundaries, so that any particular value of s occurs on at most one internal boundary. An integral with respect to s with no stated limit of integration should be understood to mean an integral over the union of all of the internal foam boundaries. With this understanding, the equations of motion are as follows:

$$\rho\left(\frac{\partial \mathbf{u}}{\partial t} + \mathbf{u} \cdot \nabla \mathbf{u}\right) = -\nabla p + \mu \nabla^2 \mathbf{u} + \mathbf{f}, \tag{4}$$

$$\nabla \cdot \mathbf{u} = 0, \tag{5}$$

$$\mathbf{f}(\mathbf{x}, t) = \int \mathbf{F}(s, t)\delta(\mathbf{x} - \mathbf{X}(s, t))ds, \tag{6}$$

$$\frac{\partial \mathbf{X}}{\partial t}(s, t) = \mathbf{u}(\mathbf{X}(s, t), t) + M\mathbf{F}\bigg/\left|\frac{\partial \mathbf{X}}{\partial s}\right| = \int \mathbf{u}(\mathbf{x}, t)\delta(\mathbf{x} - \mathbf{X}(s, t))d\mathbf{x} + M\mathbf{F}\bigg/\left|\frac{\partial \mathbf{X}}{\partial s}\right|, \tag{7}$$

$$\mathbf{F}(s, t) = \frac{\partial}{\partial s}(\gamma \boldsymbol{\tau}) = \gamma \frac{\partial \boldsymbol{\tau}}{\partial s}, \tag{8}$$

$$\boldsymbol{\tau}(s, t) = \frac{\partial \mathbf{X}}{\partial s}\bigg/\left|\frac{\partial \mathbf{X}}{\partial s}\right|. \tag{9}$$

Eqs. (4) and (5) are the familiar Navier–Stokes equations for a viscous incompressible fluid. The unknown functions in the fluid equations are the fluid velocity, $\mathbf{u}(\mathbf{x}, t)$; the fluid pressure, $p(\mathbf{x}, t)$; and the force density applied by the immersed boundary to the fluid, $\mathbf{f}(\mathbf{x}, t)$, where $\mathbf{x} = (x, y)$ are fixed Cartesian coordinates, and t is the time.

Eqs. (8) and (9) are the foam boundary equations which are written in Lagrangian form. The unknown $\mathbf{X}(s, t)$ completely describes the motion of the foam boundary and also its spatial configuration at any given time. The functions $\boldsymbol{\tau}(s, t)$ is the unit tangent vector to the foam boundary. In Eq. (8), the first formula for $\mathbf{F}(s, t)$ is the standard one for a fiber under tension, where $\mathbf{F}ds$ is the force applied by the interval ds of such a fiber to the fluid in which it is immersed. The second formula follows from the first one because the surface tension γ is constant.

An important consequence of Eqs. (8) and (9) is that the boundary force density $\mathbf{F}$ is normal to the boundary, since $\boldsymbol{\tau}$ is a unit vector Eq. (9), and it therefore follows that $\boldsymbol{\tau} \cdot \partial \boldsymbol{\tau}/\partial s = (1/2)(\partial/\partial s)|\boldsymbol{\tau}|^2 = 0$. The fact that $\mathbf{F}$ is normal to the boundary simplifies the formulation of the problem, as explained in more detail below.

Eqs. (6) and (7) both involve the two-dimensional Dirac delta function $\delta(\mathbf{x}) = \delta(x)\delta(y)$, which expresses the local character of the interaction between the fluid and boundary. Eq. (6) simply expresses the relation between the two corresponding force densities $\mathbf{f}(\mathbf{x}, t)d\mathbf{x}$ and $\mathbf{F}(s, t)ds$. Eq. (7) is the equation of motion of the immersed foam boundary in which M is the permeability constant. In order to derive Eq. (7), we start with the special case of zero permeability. When the permeability $M = 0$, Eq. (7) becomes the familiar no-slip condition. In the following, we use the notation $\mathbf{U}(s, t)$ to represent the fluid velocity evaluated at the boundary point $\mathbf{X}(s, t)$, i.e.,
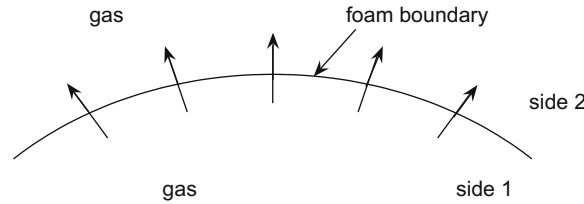
Fig. 1. A foam boundary with permeability.

$$\mathbf{U}(s,t) = \mathbf{u}(\mathbf{X}(s,t),t) = \int \mathbf{u}(\mathbf{x},t)\delta(\mathbf{x} - \mathbf{X}(s,t))d\mathbf{x}. \tag{10}$$

Now we consider the nonzero permeability of the foam boundary. (This discussion will be phrased in terms of the 2-D case, but a similar discussion could be made in the 3-D case with a few changes of units.) We assume that the gas (fluid) goes through the liquid-film boundary only in the normal direction. Consider a patch of the boundary of which the length is $|\frac{\partial \mathbf{X}}{\partial s}|ds$. The net amount of gas per unit time transported through the patch will be proportional to the pressure difference and the length of the patch. This means that the flux through the patch is equal to $M(p_1 - p_2)|\frac{\partial \mathbf{X}}{\partial s}|ds$ where M is the permeability and p_1 and p_2 are the pressures on the 2 sides of the foam boundary, see Fig. 1. We assume here that the thickness of the foam boundary is a constant. (Otherwise, the flux could also be inversely proportional to the thickness of the foam boundary.)

The flux through the patch can be also evaluated by considering the difference between the fluid velocity at the internal boundary and the velocity of the boundary itself. That is, the flux can be written as

$$\mathbf{n}(s,t) \cdot \left(\mathbf{U}(s,t) - \frac{\partial \mathbf{X}}{\partial t}(s,t)\right)\left|\frac{\partial \mathbf{X}}{\partial s}\right|ds, \tag{11}$$

where $\mathbf{n}(s,t)$ is the unit normal to the internal boundary. Setting the above two expressions for the flux equal to each other, we get

$$M(p_1 - p_2) = \mathbf{n}(s,t) \cdot \left(\mathbf{U}(s,t) - \frac{\partial \mathbf{X}}{\partial t}(s,t)\right). \tag{12}$$

From the normal component of mechanical equilibrium at the foam boundary, we see that the pressure jump $(p_1 - p_2)$ can be related to the normal component of the boundary force $\mathbf{F}(s,t)$ [11,12] as

$$(p_1 - p_2)\left|\frac{\partial \mathbf{X}}{\partial s}\right| + \mathbf{F}(s,t) \cdot \mathbf{n} = 0. \tag{13}$$

Combining these equations and using the fact that $\mathbf{F}(s,t)$ is normal to the boundary as discussed above, we obtain

$$\frac{\partial \mathbf{X}}{\partial t}(s,t) - \mathbf{U}(s,t) = M\mathbf{F}(s,t) \bigg/ \left|\frac{\partial \mathbf{X}}{\partial s}\right|. \tag{14}$$

Note that the tangential no-slip condition is automatically satisfied in Eq. (14), i.e.,

$$\left(\frac{\partial \mathbf{X}(s,t)}{\partial t} - \mathbf{U}(s,t)\right) \cdot \boldsymbol{\tau} = 0. \tag{15}$$

One can see that our IB formulation has the advantage of not needing to evaluate the pressure differences between bubbles in order to move the internal boundaries of the foam, since the relative slip between such a boundary and the fluid can be naturally found directly from the boundary force. This is important, since the pressure is only computed on the uniform grid that is used for the fluid mechanics (see next section), and the internal boundaries of the foam cut through this grid without being constrained to conform to it in any way, so the direct evaluation of the fluid pressure on the 2 sides of an internal boundary would require some sort of extrapolation procedure. This is completely avoided here, since our formulation makes no explicit reference to the pressure at all.

3. Numerical scheme

3.1. Computational procedure

What has been stated so far is the mathematical formulation of the problem in immersed boundary form (i.e., with delta-function forces instead of explicit boundary conditions). For the numerical implementation, we use a first-order IB method, generalized to take a permeable foam boundary into account [10]. As usual in IB computations, we introduce two distinct grids: a regular Eulerian grid for the fluid variables, and a Lagrangian grid to track the foam boundary. Let the fluid domain

be $\Omega = [0, L_x] \times [0, L_y]$ and let the fluid variables be defined on a fixed $N_x \times N_y$ Eulerian grid labeled as $\mathbf{x} = (x_i, y_j) = (ih, jh), 0 \leqslant i \leqslant N_x, 0 \leqslant j \leqslant N_y$, where the mesh width $h = L_x/N_x = L_y/N_y$ is uniform. For the foam boundary, we use a set of Lagrangian points $\mathbf{X}_k = \mathbf{X}(k\Delta s), 0 \leqslant k \leqslant n_f$ to track the boundary, where Δs is the discrete increment of the Lagrangian parameter s along the boundary. Recall that Δs is not arc length in general. In particular, Δs remains constant over time even though the physical length of the segment to which it refers may grow or shrink. Note in the foregoing that we have used a subscript to denote a discrete spatial location. Similarly we use a superscript to denote the time step index Thus, $\mathbf{u}^n(\mathbf{x})$ and $\mathbf{X}^n(s)$ are the approximations of $\mathbf{u}(\mathbf{x}, n\Delta t)$ and $\mathbf{X}(s, n\Delta t)$, respectively.

Throughout this section, we simplify the notation by considering only one of the internal boundaries of the foam. Since there are many such internal boundaries, the numerical procedures we describe below, in particular Steps 1, 2, and 4, need to be applied to all of them. The step-by-step procedure for the time integration from time level n to time level $n + 1$ can be summarized as follows.

Step 1 : Using the position of the internal boundary $\mathbf{X}n$, calculate the Lagrangian force density by

$$\mathbf{F}_k^n = \frac{\gamma}{\Delta s} \sum_{i=1}^{n_f-1} \frac{\mathbf{X}_{i+1}^n - \mathbf{X}_i^n}{|\mathbf{X}_{i+1}^n - \mathbf{X}_i^n|} (\delta_{i,k} - \delta_{i,k-1}), \tag{16}$$

where $\delta_{i,k}$ is the Kronecker symbol which is 1 when $i = k$ and 0 otherwise. This force density is derived from the relation $\mathbf{F}_k^n \Delta s = -\partial E/\partial \mathbf{X}_k^n$, where $E[\mathbf{X}^n]$ is the discretized energy functional of the form $E[\mathbf{X}^n] = \gamma \sum_{k=1}^{n_f-1} |\mathbf{X}_{k+1}^n - \mathbf{X}_k^n|$.

Step 2 : Distribute this tension force defined on Lagrangian grid points into the force at Eulerian spatial grid points to be applied in the Navier–Stokes equations. This is done by a discretization of Eq. (6) as

$$\mathbf{f}^n(\mathbf{x}) = \sum_k \mathbf{F}_k^n \delta_h(\mathbf{x} - \mathbf{X}_k^n)\Delta s, \tag{17}$$

where $\mathbf{x} = (x_1, x_2)$ is the fluid mesh point, and δ_h is the smooth version of Dirac delta function [11,13].

Step 3 : Given the Eulerian force density $\mathbf{f}^n(\mathbf{x})$, we are ready to solve the descritized version of the fluid equations Eqs. (4) and (5):

$$\rho \left(\frac{\mathbf{u}^{n+1} - \mathbf{u}^n}{\Delta t} + \frac{1}{2} \sum_{i=1,2} (u_i D_i^0 \mathbf{u} + D_i^0(u_i\mathbf{u}))^n \right) + \mathbf{D}p^{n+1} = L\mathbf{u}^{n+1} + \mathbf{f}^n, \tag{18}$$

$$\mathbf{D} \cdot \mathbf{u}^{n+1} = 0, \tag{19}$$

where D_i^0 is the standard central difference operator in the spatial direction denoted by i, where $i = 1, 2$, and L is the standard 5-point discrete Laplacian. Note that skew-symmetric differencing is used for the convection term [10,11,14]. The vector operator $\mathbf{D} = (D_1, D_2)$ that is used for the discrete gradient and divergence can be defined as follows [15]:

$$(D_1)\phi(x_1, x_2) = \sum_{x_1', x_2'} \phi(x_1', x_2')\gamma(x_1 - x_1')\omega(x_2 - x_2'), \tag{20}$$

$$(D_2)\phi(x_1, x_2) = \sum_{x_1', x_2'} \phi(x_1', x_2')\omega(x_1 - x_1')\gamma(x_2 - x_2'), \tag{21}$$

where $\gamma(x) = \delta_h(x + X)|_{X=-h/2}^{X=h/2}$ and $\omega(x) = \int_{h/2}^{-h/2} \delta_h(x + X)dX$. It is designed for "improved volume conservation" and is constructed according to a recipe introduced in [15] which ensures that the value of $\mathbf{D} \cdot \mathbf{u}$ at any particular grid point is exactly equal to the average over an $h \times h$ square centered on that grid point of the continuous divergence of the interpolated velocity field in which the immersed boundary points move. Note that Eqs. (18) and (19) are a linear system with constant coefficients in the unknowns $\mathbf{u}^{n+1}$ and p^{n+1}. With the periodic boundary conditions, we solve this linear system using Fourier transform methodology.

Step 4 : Update the foam boundary points which are moved at the local fluid velocity of the updated velocity field, corrected by the relative slip. This is done by approximating Eq. (7) as follows:

$$\frac{\mathbf{X}_k^{n+1} - \mathbf{X}_k^n}{\Delta t} = \sum_{\mathbf{x}} \mathbf{u}^{n+1}(\mathbf{x})\delta_h(\mathbf{x} - \mathbf{X}_k^n)h^2 + \frac{M\mathbf{F}_k^n\Delta s}{(|\mathbf{X}_{k+1}^n - \mathbf{X}_k^n| + |\mathbf{X}_k^n - \mathbf{X}_{k-1}^n|)/2}. \tag{22}$$

This completes the time step.

3.2. Some implementation details

(A) No permeability at the junctions: We assume that there is no permeability at the junctions where three (or more) internal boundaries meet, i.e., at $k = 1$ or at $k = n_f$. These junctions simply move at the local fluid velocity, that is, by Eq. (22) with $M = 0$. To allow permeability at the junction points would result in inconsistencies, since the normal direction is not

uniquely defined there. Physically, the lack of permeability at junction points is enforced by an accumulation of liquid at such points, resulting in a slight thickening and smoothing out of the junction. An interesting mathematical consequence of the assumption that there is no permeability at the junction itself is that, by continuity, the flux through an internal boundary must approach zero as a junction is approached. This can only happen if the pressure difference, and hence the curvature, approaches zero as the junctions are approached. Thus our internal boundaries are locally flat at their end points. This does not need to be imposed as a boundary condition, since deviations from such local flatness will be automatically corrected by the dynamics of the numerical scheme.

(B) The maintenance of foam boundary point resolution: Since the internal boundary points $\mathbf{X}_k^n$ of the foam move without any constraint on the distance between two adjacent points, we need to address the important issue how to maintain reasonable resolution along the boundary. If the resolution becomes too coarse, there will be leaks between the boundary points, and if it becomes too fine, there will be too severe a constraint on the time step to maintain numerical stability. We maintain proper resolution of the boundary by simply adding or deleting immersed boundary points as needed in the following way.

At each time step, we start from one end point of an internal boundary and proceed along that boundary to check the distances between neighboring boundary points $\mathbf{X}_{k+1}^n$ and $\mathbf{X}_k^n$. Whenever $|\mathbf{X}_{k+1}^n - \mathbf{X}_k^n| > h/2$, we create a new immersed boundary point halfway between them. Note that the addition of such a point does not change the length of the immersed boundary at all, and therefore it has no effect on the potential energy of the boundary. Whenever $|\mathbf{X}_{k+1}^n - \mathbf{X}_k^n| < h/4$, we delete both points and create in their place a new boundary point halfway between them. An exception to this rule is that the end points of an internal boundary are never deleted. When a neighboring point to an end point is within the lower-limit distance of the end point ($h/4$), the neighboring point is simply deleted. Unlike addition of points, deletion does slightly change the potential energy of the boundary, but only by lowering it. Thus, deletion may be viewed as a kind of numerical dissipation of energy. This loss of energy is part of the numerical error of the scheme.

(C) Implementation of no-slip boundary conditions by applying a boundary feedback force: To complete the description of the numerical IB method, we need to explain the boundary conditions imposed along the edges of our computational domain. As discussed before, we use periodic boundary conditions in both space directions for the fluid equations. Despite this, we are able to impose the no-slip condition at the edges of the computational domain by laying out an array of "target points" along those boundaries. Let $\mathbf{Z}(s, t)$ be the target points along the boundaries, then the method used to impose no-slip condition is to apply to the boundary by the following force:

$$\mathbf{F}_0(s, t) = c_0(\mathbf{Z}(s, t) - \mathbf{X}(s, t)), \tag{23}$$

where c_0 is a large constant and $\mathbf{X}(s, t)$ is immersed boundary points that moves at the local fluid velocity and applies $\mathbf{F}_0(s, t)$ locally to the fluid. This provides a feedback mechanism for computing the boundary force needed to enforce the no-slip condition. In the present paper, the target points $\mathbf{Z}(s, t)$ are sometimes fixed (i.e., independent of time), to simulate stationary walls, and sometimes they move along the boundaries of the domain in a prescribed manner to simulate sliding walls. Note that the target-point method for enforcing the no-slip condition still allows for the usage of FFT, since we do so not by changing the boundary conditions per se but instead by applying forces that effectively prevent the fluid from moving, or force it to move in a prescribed manner at the specified locations.

4. Results and discussion

In this section, we perform three different numerical tests for our model and numerical scheme presented in the previous sections. They include: (1) a foam with a single inner cell, (2) a numerical verification and convergence study, and (3) a foam with multiple inner cells. Throughout this paper, we choose the computational domain $\Omega = [0, 1] \times [0, 1]$, and no-slip boundary conditions are imposed along the computational boundary, unless otherwise stated. The fluid density is chosen as $\rho = 1$, the viscosity $\mu = 0.001$, and the surface tension coefficient $\gamma = 2$. Note that these parameters are arbitrarily chosen and do not correspond to any particular physical case. We use three different permeabilities, $M = 0$, 0.025, and 0.05 to see how the permeability affects the foam dynamics.

4.1. Foam with a single inner cell

As the first test, we start with a single *n*-edged inner cell with circular arcs and connect its vertices with *n* straight radial lines to the computational boundary as illustrated in Fig. 2. Thus, the initial foam boundary is the combination of a circle with radius 0.2 and *n* straight lines. Fig. 2 shows the case of $n = 8$, and we shall later change the number *n*. Note that, the number of lines is the same as the number of vertices (triple junctions) of the inner cell, which is initially a circular disc. We use the mesh width $h = \Delta x = \Delta y = 1/256$, which is uniform and fixed in time, and the time step duration $\Delta t = 2.5 \times 10^{-6}$.

Fig. 3 compares the configurations of the foams at selected times: $t = 0$ (dotted lines), $t = 0.25$ (dashed lines), and $t = 0.5$ (solid lines). The permeability M is zero in the upper panels and $M = 0.05$ in the lower panels. The number of edges of the central cell is $n = 4$ (first column), $n = 6$ (second column), and $n = 8$ (third column), respectively. In the case of zero permeability, $M = 0$, all the foams quickly go to their steady configurations and almost stop moving. When the permeability
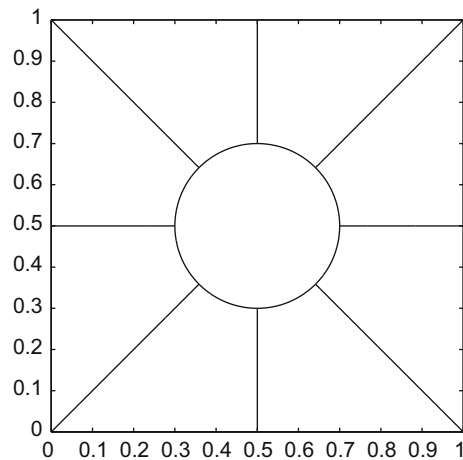
Fig. 2. Initial foam boundary as a combination of a circle with radius 0.2 and 8 straight lines which connect the circle to the computational boundary.
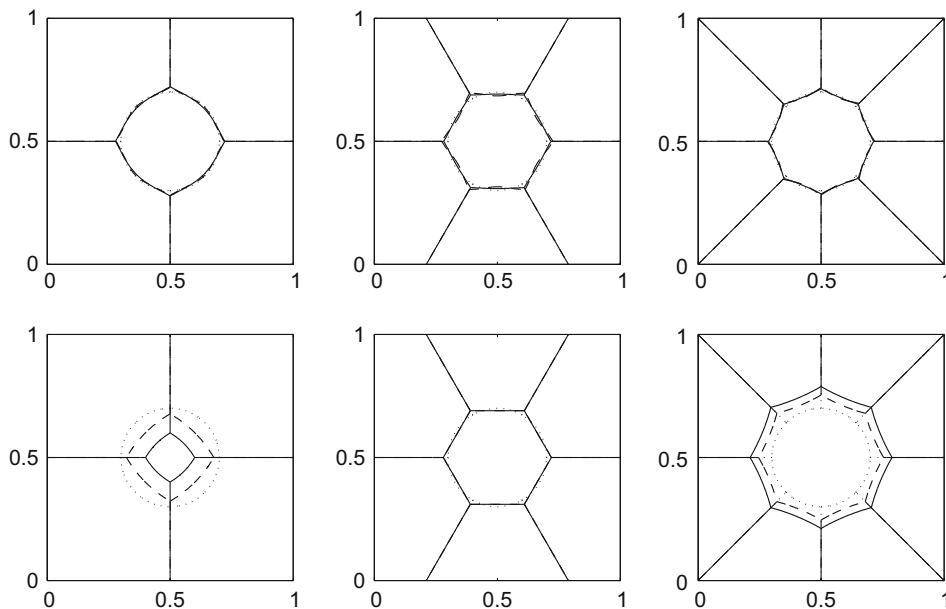

Fig. 3. Motion of the foam boundaries. The permeability is $M = 0$ in the upper panels and $M = 0.05$ in the lower panels. The number of edges of the central bubble is $n = 4$ (first column), $n = 6$ (second column), and $n = 8$ (third column), respectively. The times chosen are $t = 0$ (dotted lines), $t = 0.25$ (dashed lines), and $t = 0.5$ (solid lines).

$M = 0.05$, the inner cell of 4 edges shrinks, that of 8 edges grows, and that of 6 edges behaves very much as if there were no permeability. This observation from Fig. 3 confirms the von Neumann relation (3) qualitatively.

Since our computation is based on fluid mechanics, we can obtain the fluid velocity field as well as the motion of the foam's internal boundaries. Fig. 4 shows the streamlines of the velocity fields. The case in each panel corresponds to that in Fig. 3. The time is fixed at $t = 0.5$. When the central bubble is 4-sided (left column), the vertices are moving inward. In the case of zero permeability (upper left), this is necessarily compensated by outward motion of the centers of the edges, but in the case of nonzero permeability (lower left), the central bubble as a whole is collapsing inwards. The opposite behavior is seen in the case of an 8-sided central bubble (right column), in which the vertices are moving outward. With no permeability (upper right) the outward motion of the vertices is compensated by inward motion of the centers of the edges, but in the case of positive permeability (lower right) the whole central bubble is expanding. The 6-sided central bubble maintains its area regardless of permeability (see below for quantitative evidence of this). Nevertheless, its flow pattern has different symmetry in the impermeable and permeable cases (compare the upper and lower panels in the middle column of Fig. 4).
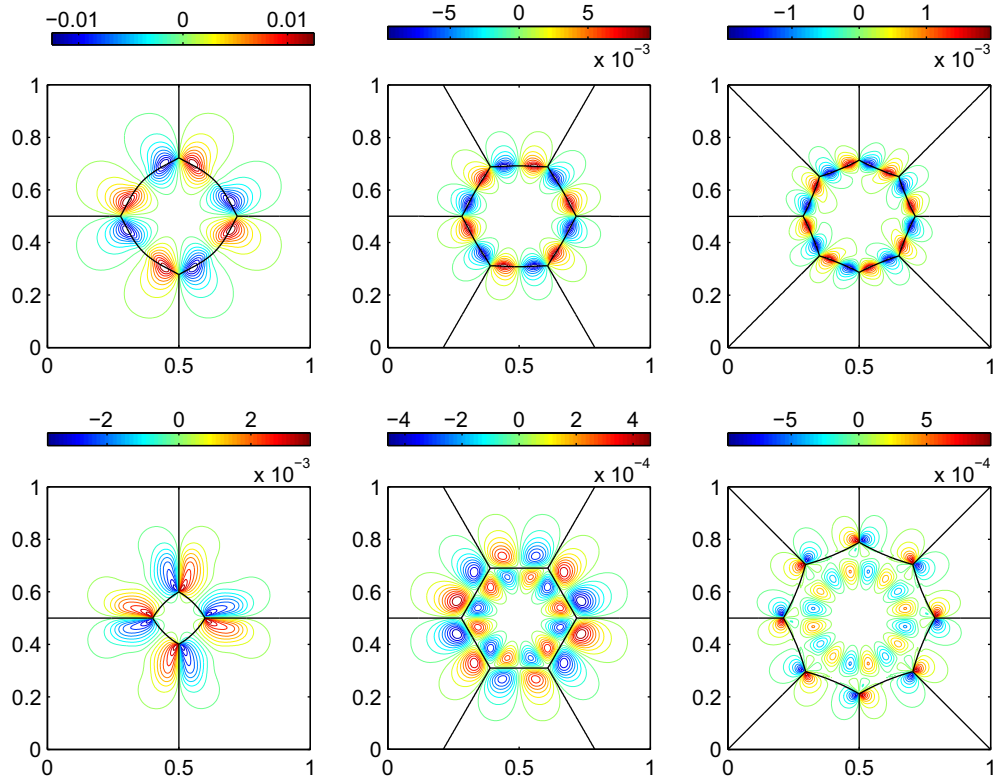
Fig. 4. Streamlines of the velocity fields at time $t = 0.5$. The case in each panel corresponds to that in Fig. 3.

In order to check the von Neumann relation quantitatively, we change the number of cell edges and the permeability parameter and plot the areas of the inner cells as functions of time in Fig. 5. The number of edges varies from $n = 4$ to $n = 9$, and the permeability parameters are $M = 0$ (left panel), $M = 0.025$ (middle panel), and $M = 0.05$ (right panel). The inner cell is initially a circular disc. When there is no permeability ($M = 0$), the areas of the inner cells do not change for all the numbers n of edges. When the permeability is nonzero, the areas of the inner cells change for any number of edges except for the case of $n = 6$. These plots of the inner cell area are all linear as functions of time and almost follow the von Neumann relation (Eq. (3)), i.e., $\frac{dA}{dt} = -2\pi M\gamma(1 - n/6)$, which is represented by the solid lines in the figure.

4.2. Numerical verification and convergence study

Even though the changes of the inner cell areas are very close to those predicted by the von Neumann relation, we can see some discrepancy: see Fig. 5 and compare the solid lines to the other lines. The origin of most of this discrepancy is that the initial shapes of the foams in Fig. 3 do not satisfy all of the assumptions used in deriving the von Neumann relation. Whereas the von Neumann relation assumes that the angles at triple junctions should be $2\pi/3$, one of the three initial angles at each of those junctions in our case is π and the other two are $\pi/2$. This discrepancy will be quickly corrected (in principle, infinitely quickly) but the resulting boundary layer in time introduces a certain error.

In order to remove the initial transition and check the von Neumann relation more carefully, we construct foams which have the initial shape satisfying the assumption that the angles at triple junctions are $2\pi/3$. Fig. 6 shows the motion of two such foams, each at two different times: 4-edged (left) and 8-edged (right), with the initial configuration of the inner cell depicted by a dotted line in each case. The solid lines show the configurations of the two foams at $t = 0.1$. The permeability coefficient is fixed at $M = 0.05$. Note that the 4-sided inner cell shrinks whereas the 8-sided inner cell grows. Now we choose the mesh sizes of the domain $N = 128, 256, 512$, and 1024 so the corresponding mesh width is $h = 1/N$. We also choose Δs and Δt proportional to h, so that each factor of 2 in refinement of the fluid mesh width is accompanied by a factor of 2 refinement of the boundary mesh and likewise of the time step duration. Fig. 7 shows the errors of the computed areas of the inner cells from the von Neumann relation in the two cases. The errors are plotted as functions of time on a logarithmic vertical scale for each of the cases $N = 128, 256, 512$, and 1024. Clearly the discrepancy between the computed areas and those predicted by von Neumann is decreasing as $N \to \infty$.

Next, we study the convergence of the computed solution. Since we do not know the exact solution of the problem, the estimation of a convergence ratio requires three numerical solutions for three consecutive N's. Let (u_N, v_N) be the velocity
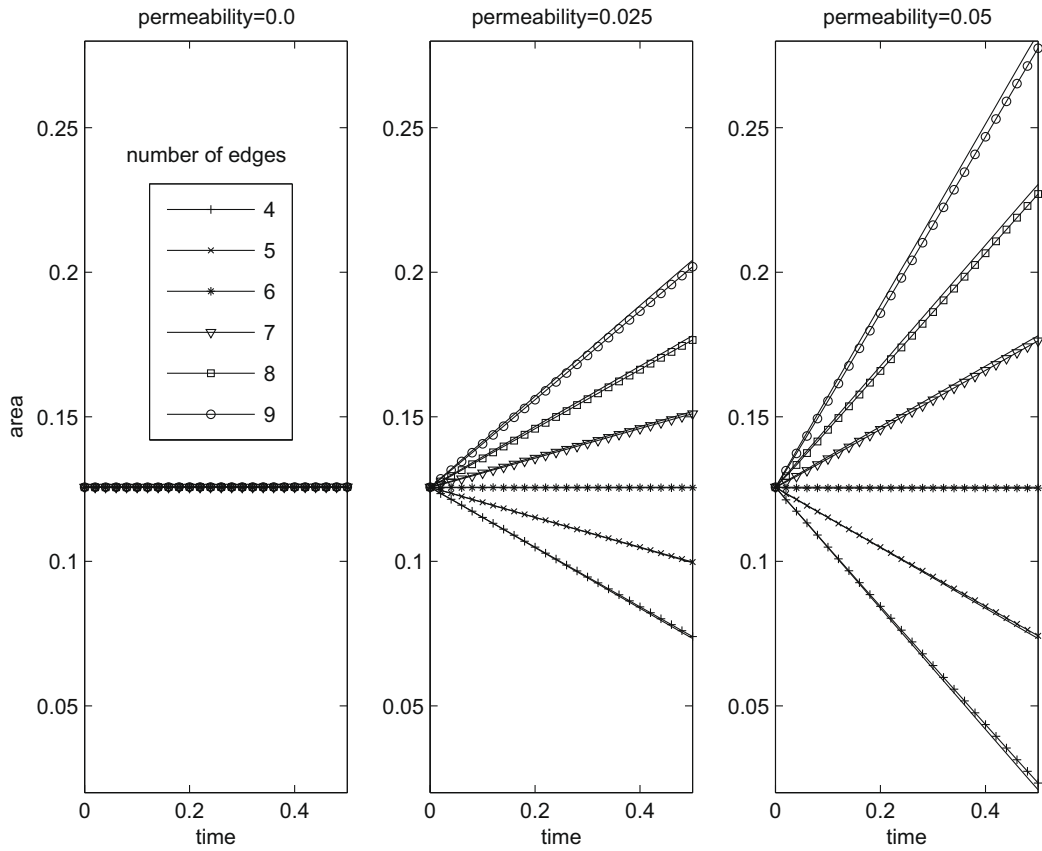
Fig. 5. The change of the inner cell area with time. The number of edges varies from $n = 4$ to $n = 9$, and the permeability parameters are $M = 0$ (left), $M = 0.025$ (middle), and $M = 0.05$ (right). The changes of the inner cell areas are linear and almost follow the von Neumann relation, which is represented by the solid lines.
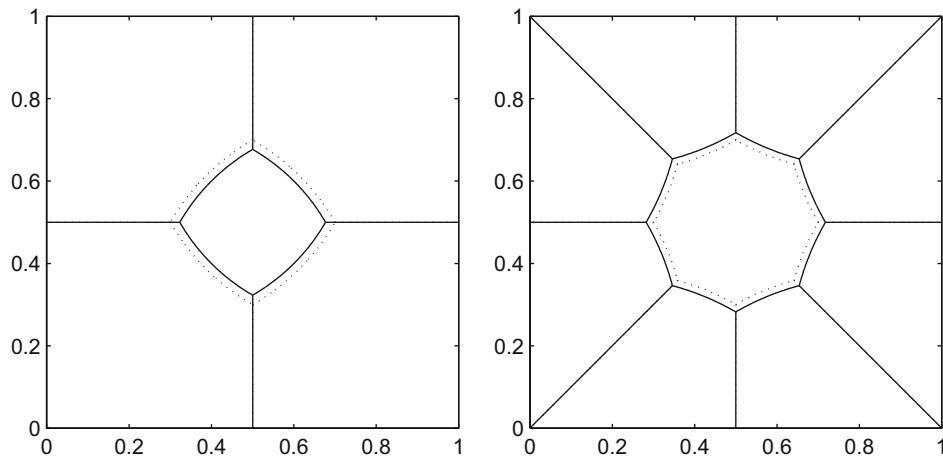

Fig. 6. Foam boundary of 4-edged (left) and 8-edged (right) inner cells. The times are $t = 0$ (dotted line) and $t = 0.1$ (solid line).

field, and let $\| \cdot \|_2$ be the L_2 norm. The top panel of Fig. 8 shows the convergence ratios $(\|u_N - u_{2N}\|_2^2 + \|v_N - v_{2N}\|_2^2)^{1/2}/(\|u_{2N} - u_{4N}\|_2^2 + \|v_{2N} - v_{4N}\|_2^2)^{1/2}$ as functions of time for each of the cases $N = 128$ (dotted line) and 256 (solid line). The convergence ratio 2 implies that the scheme has first-order accuracy which is typical of the IB method as applied to problems with thin elastic boundaries (for second order convergence of the IB method in the case of an immersed elastic structure of finite thickness, see [16,17]).
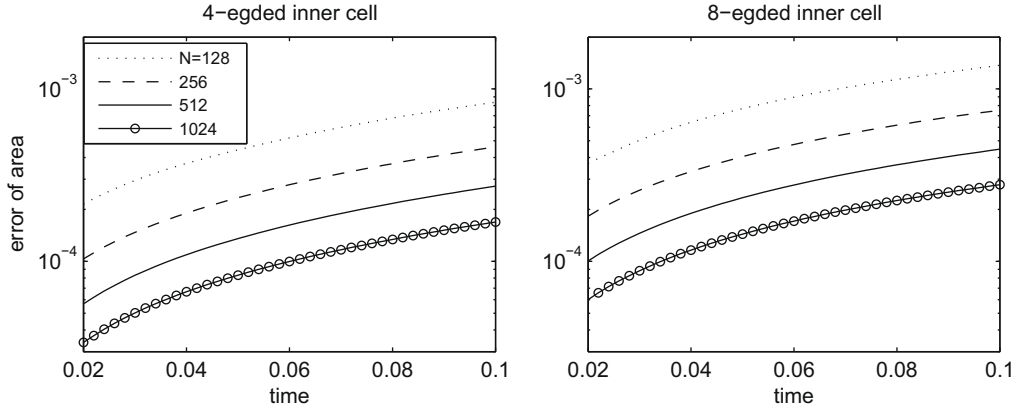
Fig. 7. The errors of area in comparison to that predicted by the von Neumann relation are plotted as functions of time on a logarithmic vertical scale for each of the cases N

The bottom panel of Fig. 8 shows the convergence ratios of the motion of the vertices of the foam as functions of time. Let (x_N^i, y_N^i) be the position of vertices of the inner cell where the index $i = 1, 2, \ldots, I$ is the numbering of the vertices. Thus $I = 4$ for the 4-sided inner cell and $I = 8$ for the 8-sided inner cell. Then the bottom panel of Fig. 8 shows the convergence ratios $\left(\sum_{i=1}^{I} [(x_N^i - x_{2N}^i)^2 + (y_N^i - y_{2N}^i)^2] \right)^{1/2} \Big/ \left(\sum_{i=1}^{I} [(x_{2N}^i - x_{4N}^i)^2 + (y_{2N}^i - y_{4N}^i)^2] \right)^{1/2}$ as functions of time for each of the cases $N = 128$ (dotted line) and 256 (solid line). Again we can see that the actual convergence ratios are roughly equal to 2, which implies that the scheme is approximately first-order accurate.

4.3. Foam with multiple inner cells

We now consider more general foam configurations with a fixed permeability, $M = 0.05$. The first case, shown in Fig. 9, has three inner cells with different numbers of sides ($n = 4$, 6, and 8) in a fluid-filled domain $\Omega = [0, 2] \times [0, 1]$. At the outer boundary, no-slip boundary conditions are imposed by means of target points, in the manner discussed above. The upper panels show the configuration of the foam at $t = 0$ (left) and $t = 0.5$ (right). Streamlines of the velocity field at the latter time are also shown (the fluid is at rest at $t = 0$, so no streamlines appear in that case). The lower panel of Fig. 9 shows the areas of

the three inner cells plotted as functions of time, in comparison to the areas predicted by the von Neumann relation. As before, the agreement is excellent, and the small discrepancy seen in the figure is mostly attributable to the failure of the initial configuration to satisfy the equal-angle rule, as discussed above. The linear changes in area with time over a wide range of areas makes it clear that the rate of change of area is unrelated to the area per se. For example, the 8-sided cell in Fig. 9 grows when it is the smallest of the three inner cells, and continues to grow at exactly the same rate when it is the largest of the three at later time.

The fluid dynamics of a foam is not necessarily restricted to the slow coarsening regime that has been considered up to now. To illustrate this, we use the same initial configuration of the foam as in Fig. 9. We remove the target points on the side boundaries, however, so that the foam is periodic in the x-direction. We keep fixed target points on the bottom of the domain. Near the top of the domain, at $y = 0.875$, we create a horizontal row of target points that slides left and right in an oscillatory manner. This motion of the target points can be created by defining $\mathbf{Z}(s, t) = (s + A\sin(\omega t), 0.875)$ for $0 \leqslant s \leqslant 2$ in Eq. (23) where the amplitude is $A = 0.25$ and frequency is $\omega = 10\pi$. The upper panels of Fig. 10 show the motion of the foam with the streamlines of the velocity fields at $t = 0.25$ (left) and $t = 0.5$ (right). We can clearly observe the interaction between the foam boundaries and the fluid flow. Even though the foam is now far from equilibrium, the areas of the inner cells still follow closely the von Neumann relation, see the lower panel of Fig. 10.

Finally we simulate the coarsening of a more complicated foam immersed in the domain $\Omega = [0, 1] \times [0, 1]$. Fig. 11 shows the motion of the foam at some chosen times. We initially set up the inner cells with different numbers of edges ranging from $n = 3$ to $n = 9$, and number those inner cells accordingly at initial time. We can see that the cells with fewer than six edges shrink and disappear as time goes on: The 3-sided cell disappears at $t = 0.12$, the 4-sided cell at $t = 0.24$, and the 5-sided cell at $t = 0.48$. Meanwhile, the other cells with fewer than 6 edges (not numbered) are also decreasing in area. At the same time, however, the cells with more than 6 edges are growing in area, see for example the panel at time $t = 0.48$. The overall result of these changes in area is the coarsening of the foam structure.
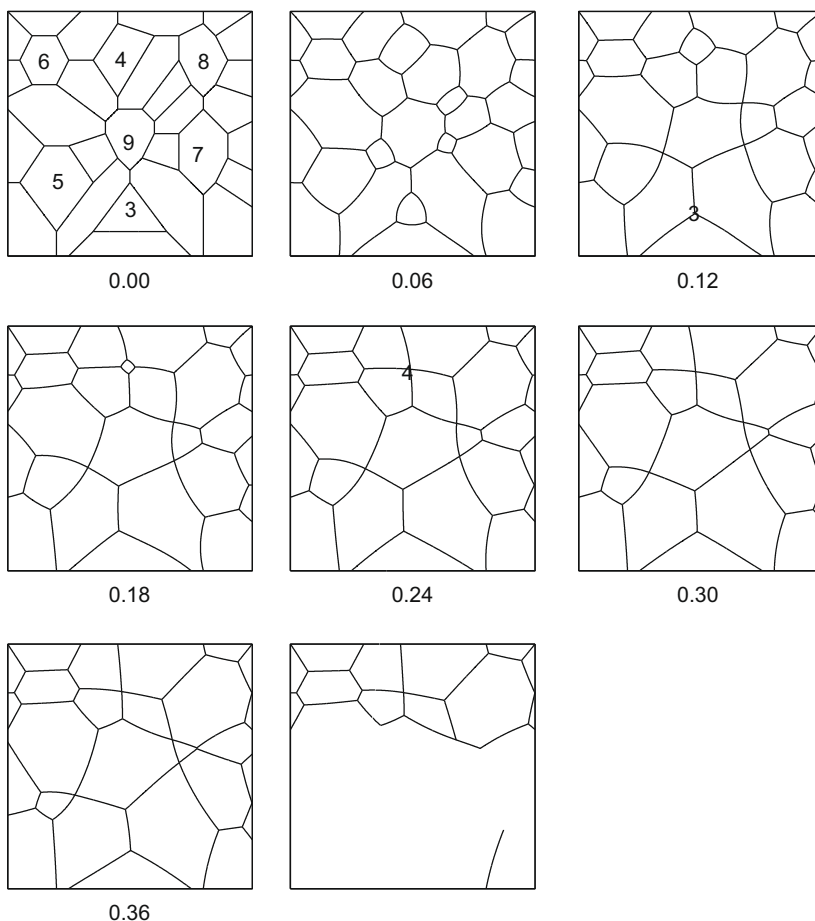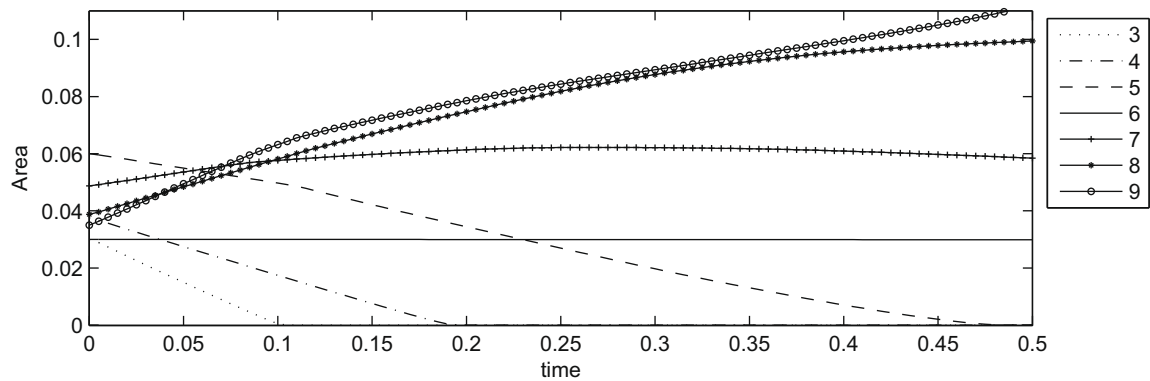
Fig. 12. The areas of the numbered cells in Fig. 11 as functions of time.

Whereas the cells with numbers of edges other than six change their shapes and areas, the cell with six edges changes only its shape with its area remaining constant, see the cell numbered 6 in Fig. 11. In order to see more quantitatively the changes of the cell areas, we plot in Fig. 12 the areas of the inner cells numbered in Fig. 11 as functions of time. The area of the 6-sided cell does not change, the areas of the cells with fewer than 6 edges decrease, and the areas of the cells with more than 6 edges increase. The cell areas as functions of time do not, however, follow the von Neumann relation exactly, since their slopes are not constant after about $t = 0.1$.

We attribute these deviations from linearity to the total shrinkage of some cells and to the new generation of quadruple junctions, see the figure at time $t = 0.12$ when this happens for the first time. At a quadruple junction, the exterior angles are no longer equal to $2\pi/6$, as was assumed in the derivation of the von Neumann relation.

The occurrence of quadruple junctions points out a limitation of our present methodology. In reality, quadruple junctions are unstable and resolve themselves into a pair of triple junctions, with the creation of a new edge that arises at zero length and grows in length as the two triple junctions move apart. We do not currently simulate this phenomenon, however. Thus, when a quadruple (or higher-order) junction forms in the course of our simulations it remains as such, unless it collides with another junction, in which case its order becomes even higher. The resolution of higher-order junctions into lower order ones is left as a subject for future work.

5. Summary and conclusions

We have presented an immersed boundary method to simulate the fluid dynamics of a two-dimensional dry foam. We model the gas phase of the foam as a viscous incompressible fluid, and the liquid phase as a massless network of permeable internal boundaries under surface tension. The internal boundary force, generated by the surface tension, is everywhere normal to the internal boundaries. Permeability is modeled by allowing the internal boundaries to slip relative the fluid, at a velocity (speed *and* direction) proportional to the boundary force. This is equivalent to slip in the normal direction only at a speed proportional to the pressure difference across each internal boundary, and thus models correctly the diffusion of gas through the liquid phase of the foam.

An algorithm is described that maintains the resolution of each internal boundary within predetermined bounds despite arbitrarily large changes in length of the internal boundary.

We have validated the method by checking that the von Neumann relation is well satisfied, except when the assumptions under which it was derived are violated. A striking fact, confirmed by our results, is that the derivation of the von Neumann relation does *not* require the assumption of uniform curvature along each internal boundary, and therefore does not require uniform pressure within each bubble of the foam. The von Neumann relation therefore remains valid in dynamical situations with nontrivial fluid dynamics in the gas phase of the foam, as we have seen. Additional validation has been provided in the form of a convergence study, which confirms the expected first-order accuracy of the scheme.

Within the context of two-dimensional foams, the principal limitation of the method as currently implemented is that we do not allow for the resolution of quadruple or higher-order junctions into triple junctions. A more important limitation, of course, is the restriction to the two-dimensional case. The extension of the methodology introduced here to the study of three-dimensional foams will be the subject of future work.

Acknowledgments

References

[1] D. Weaire, S. Hutzler, The Physics of Foams, Oxford University Press, 1999.
[2] J. von Neumann, in: C. Herring (Ed.), Metal Interfaces, American Society for Metals, Cleveland, 1952, pp. 108–110.
[3] W.W. Mullins, in: W.D. Robertson, N.A. Gjostein (Eds.), Metal Surfaces: Structure, Energetics, and Kinetics, American Society for Metals, Metals Park, Ohio, 1963, pp. 17–66.
[4] R.D. MacPherson, D.J. Srolovitz, The von Neumann relation generalized to coarsening of three-dimensional microstructures, Nature 446 (26) (2007) 1053–1055.
[5] S. Hilgenfeldt, A.M. Kraynik, S.A. Koehler, H.A. Stone, An accurate von Neumann's law for three-dimensional foams, Phys. Rev. Lett. 86 (12) (2001) 2685–2688.
[6] T. Herdtle, H. Aref, Numerical experiments on two-dimensional foam, J. Fluid Mech. 241 (1992) 233–260.
[7] X. Li, H. Zhou, C. Pozrikidis, A numerical study of the shearing motion of emulsions and foams, J. Fluid Mech. 286 (1995) 379–404.
[8] I.B. Bazhlekov, P.D. Anderson, H.E.H. Meijer, Nonsingular boundary integral method for deformable drops in viscous flows, Phys. Fluids 16 (4) (2004).
[9] A.M. Kraynik, D.A. Reinelt, Foam microrheology: from honeycombs to random foams, in: Proceedings of thePPS-15, 1999.
[10] Y. Kim, C.S. Peskin, 2-D parachute simulation by the immersed boundary method, SIAM J. Sci. Comput. 28 (6) (2006).
[11] C.S. Peskin, The immersed boundary method, Acta Numer. 11 (2002) 479–517.
[12] M.-C. Lai, Z. Li, A remark on jump conditions for three-dimensional Navier–Stokes equations involving an immersed moving membrane, Appl. Math. Lett. 14 (2001) 149–154.
[13] C.S. Peskin, D.M. McQueen, Fluid dynamics of the heart and its valves, in: Case studies in Mathematical Modeling: Ecology, Physiology, and Cell Biology, Prentice Hall, Englewood Cliffs, NJ, 1996, pp. 309–337.
[14] M.-C. Lai, C.S. Peskin, An immersed boundary method with formal second-order accuracy and reduced numerical viscosity, J. Comput. Phys. 160 (2000) 705–719.
[15] C.S. Peskin, B.F. Printz, Improved volume conservation in the computation of flows with immersed elastic boundaries, J. Comput. Phys. 105 (1993) 33–46.
[16] Y. Kim, C.S. Peskin, Penalty immersed boundary method for an elastic boundary with mass, Phys. Fluids 19 (5) (2007).
[17] B.E. Griffith, C.S. Peskin, On the order of accuracy of the immersed boundary method: higher order convergence rates for sufficiently smooth problems, J. Comput. Phys. 208 (2005) 75–105.